Promoting body carriers migration of CdS nanocatalyst by N-doping for improved hydrogen production under simulated sunlight irradiation

Wei Li [a,*], Fei Wang [a], Xiao-yun Liu [a], Yan-yan Dang [a], Jia-yuan Li [a], Teng-hao Ma [a], Chuan-yi Wang [b]

[a] College of Chemistry and Chemical Engineering, Shaanxi Key Laboratory of Chemical Additives for Industry, Shaanxi University of Science & Technology, Xi'an, Shaanxi 710021, China
[b] School of Environmental Sciences and Engineering, Shaanxi University of Science & Technology, Xi'an, Shaanxi 710021, China

ARTICLE INFO

ABSTRACT

Cadmium sulfide (CdS) has been extensively employed to achieve highly efficient H_2 production under visible-light irradiation due to its features of narrow bandgap and appropriate conduction band position. However, fast carriers recombination and severe photocorrosion inevitably result in low carriers utilization, leading to undesirable photocatalytic performance and poor durability. To address the issues, N heteroatoms were introduced into the lattice of hexagonal CdS NPs to prepare the N-doped CdS (N-CdS) nanocatalyst via a wet chemical precipitation coupled with a hydrothermal process. Due to the synergetic promotion of heteroatom-semiconductor coordination (HSC) interaction to body carriers migration of CdS, their recombination behavior was effectively hampered, resulting obviously increased photocurrent density ($\sim$2 times) and significantly improved photoexcited carriers utilization. Thereby, high apparent quantum yield (AQY = 32.41%, λ = 500 nm) was achieved by the optimized $N_{0.2}$-CdS nanocatalyst. Under simulated sunlight (SSL) irradiation, about 3983.4 $\mu mol \cdot h^{-1} \cdot g^{-1}$ of HER rate with excellent photostability was achieved at absence of cocatalyst, which raises to about 9-fold greater than that of bare CdS NPs. Moreover, density functional theory (DFT) calculations proved that the energy barrier of water splitting on Cd sites and $|\Delta G_{H^*}|$ of H_2 generation on S sites were reduced obviously due to the synergetic HSC interaction, which thermodynamically accelerated the H_2 generation. This study provides a simple and green strategy for gaining highly stable CdS photocatalyst with improved HER photoactivity.

1. Introduction

In order to alleviate the exhaustion of traditional fossil energies and promote the green and sustainable development, it is essential to exploit alternative eco-friendly energies [1]. Solar-driven technology is identified as a promising approach to achieve solar energy-to-chemical energy conversion, such as the production of CO [2], CH_3OH [3], CH_4 [4], C_2H_6 [5], H_2 [6], etc. Especially, hydrogen is considered as the ideal candidate in view of its advantages of high added-value, green sustainability, low density, easy storage, etc. [7]. However, low conversion efficiency of solar-driven technology dramatically restricts its application in practical H_2 production [8], thereby developing high-efficient photocatalysts for H_2 production has become the focus of photocatalysis field. In order to enhance light-harvesting of semiconductor photocatalysts and accelerate the separation and migration of carriers, extensive efforts have

been devoted to improve traditional photocatalysts, including heteroatom doping [9], plasma injection [10], heterojunction construction [11], structural regulation [12], etc.

Transition metal sulfides (TMSs) are deemed as the ideal photocatalytic materials for H_2 production in view of the inherent advantages of narrow bandgap and broadband light harvesting [13]. Particularly, cadmium sulfide (CdS) has attracted much attention due to its features of narrow bandgap ($\sim$2.40 eV) and appropriate conduction band position (E_{CB}), thereby it has been extensively employed to achieve highly efficient H_2 production under visible-light irradiation [14]. However, fast carriers recombination and severe photocorrosion inevitably result in low carriers utilization, leading to undesirable photocatalytic performance and poor durability [15]. Therefore, many efforts have been devoted to address above critical issues. For example, Feng et al. prepared a Pt atoms deposited black phosphorus/CdS heterostructure [16],

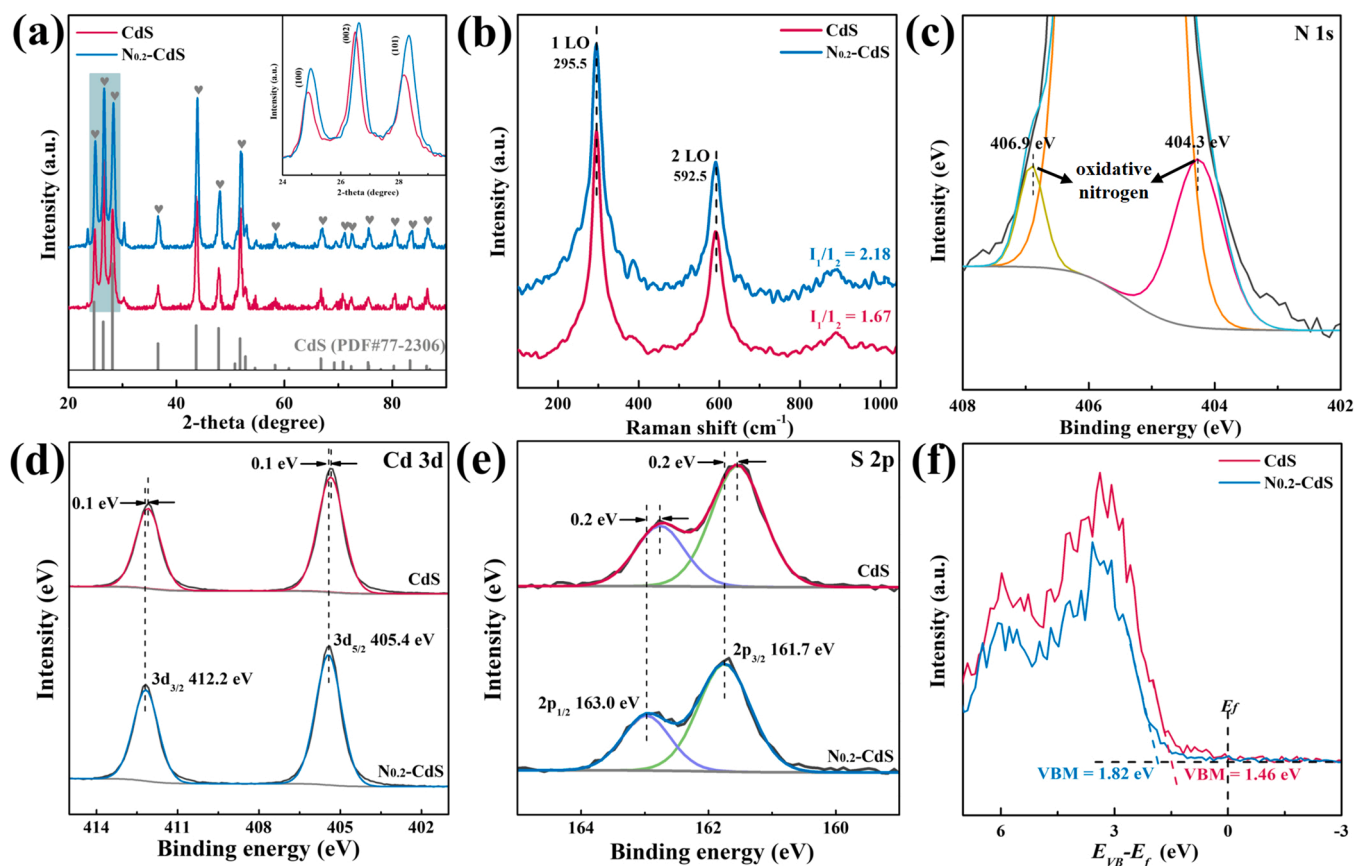**Fig. 1.** (a) XRD patterns, (b) Raman spectra, ((d)-(e)) Cd 3d and S 2p XPS core-level spectra and (f) XPS-VBs spectra of CdS and $N_{0.2}$-CdS. (c) N 1s XPS core-level spectrum of $N_{0.2}$-CdS.

Chen et al. integrated lanthanide-transition-metal clusters onto CdS Surfaces [17], and Xiang et al. reported a Sn atoms decorated CdS quantum dots [18]. Apparently, aforementioned strategies effectively facilitate carriers separation and migration, achieving highly enhanced HER activities.

In view of the practical application requirement, acquiring high-efficient photocatalytic performance by the simple and low-cost operation procedure is worth to be concerned extensively. Heteroatom doping is a simple and effective strategy to promote body carriers migration and achieve high quantum yield due to the synergetic electronic effect of heteroatom sites in body structure.[19] For example, Shi et al. synthesized a Se-doped CdS QDs with higher Fermi level position [20], Shi et al. reported a strategy to fabricate P-doped CdS with more S vacancies [21], and Zubair et al. doped C element to CdS to suppress the influence of mechanical tension and photocorrosion to its photocatalytic performance [22]. Compared with metal doping, non-metallic atoms with high electronegativity can form strong coordination interaction with metal atoms in semiconductor, effectively modulating the band structure and improving the migration behavior of carriers, thereby it will dramatically boost body carriers migration and hamper their recombination. Due to the increased effective active sites, highly improved photoactivity with excellent durability can be achieved by the doped semiconductor photocatalyst.

Inspired by this opinion, N heteroatoms were introduced into the lattice of hexagonal CdS NPs to synthesize the N-doped CdS nanocatalyst via a two-step approach. Due to the synergetic promotion of body carriers migration by HSC interaction, the recombination behavior of photoexcited carriers was effectively hampered, resulting obviously increased photocurrent density (~2 times) and significantly improved carriers utilization. Thereby, high AQY (32.41%, 500 nm) was achieved by the optimized $N_{0.2}$-CdS nanocatalyst. Under SSL-irradiation, about

3983.4 $\mu mol \cdot h^{-1} \cdot g^{-1}$ of HER rate with excellent durability was presented on this improved nanocatalyst at absence of cocatalyst, which is about 9-fold greater than that of bare CdS NPs (442.6 $\mu mol \cdot h^{-1} \cdot g^{-1}$). Moreover, DFT calculations proved that N doping obviously reduced the energy barrier of water splitting on Cd sites and Gibbs free energy change of hydrogen proton (H*) intermediates adsorption ($|\Delta G_{H*}|$) on S sites, which thermodynamically accelerated the processes of water splitting and H_2 generation. This study provides a simple and green strategy for gaining highly stable CdS photocatalyst with improved HER photoactivity.

2. Experimental section

2.1. Synthesis of N_x-CdS nanocatalysts

The CdS nanocatalysts with different N heteroatom dosages were synthesized via a two-step approach. In detail, 1.320 g $Na_2S \cdot 9H_2O$ (A.R.) and 1.355 g $Cd(Ac)_2 \cdot 2 H_2O$ (A.R.) were respectively dissolved in 80 mL deionized (DI) water, then 0.2 g urea (A.R.) was added to $Cd(Ac)_2$ solution to form a uniform mixed solution under vigorous stirring. Subsequently, Na_2S solution was slowly added to above mixed solution to form a uniform yellow gel dispersion. After aging for 12 h, the yellow sample was gained through suction filtration. Then, the collected sample was redispersed in 80 mL DI water and treated for 5 h in an autoclave (100 mL) at 180 °C. After cooling, the product was collected by centrifugation and rinsed several times with DI water, and the yellow powder ($N_{0.2}$-CdS) was gained after drying for 12 h in a vacuum freeze-dryer. Additionally, 0.1 g and 0.3 g were respectively added to $Cd(Ac)_2$ solution, and the powdered $N_{0.1}$-CdS and $N_{0.3}$-CdS were synthesized by the same operation.
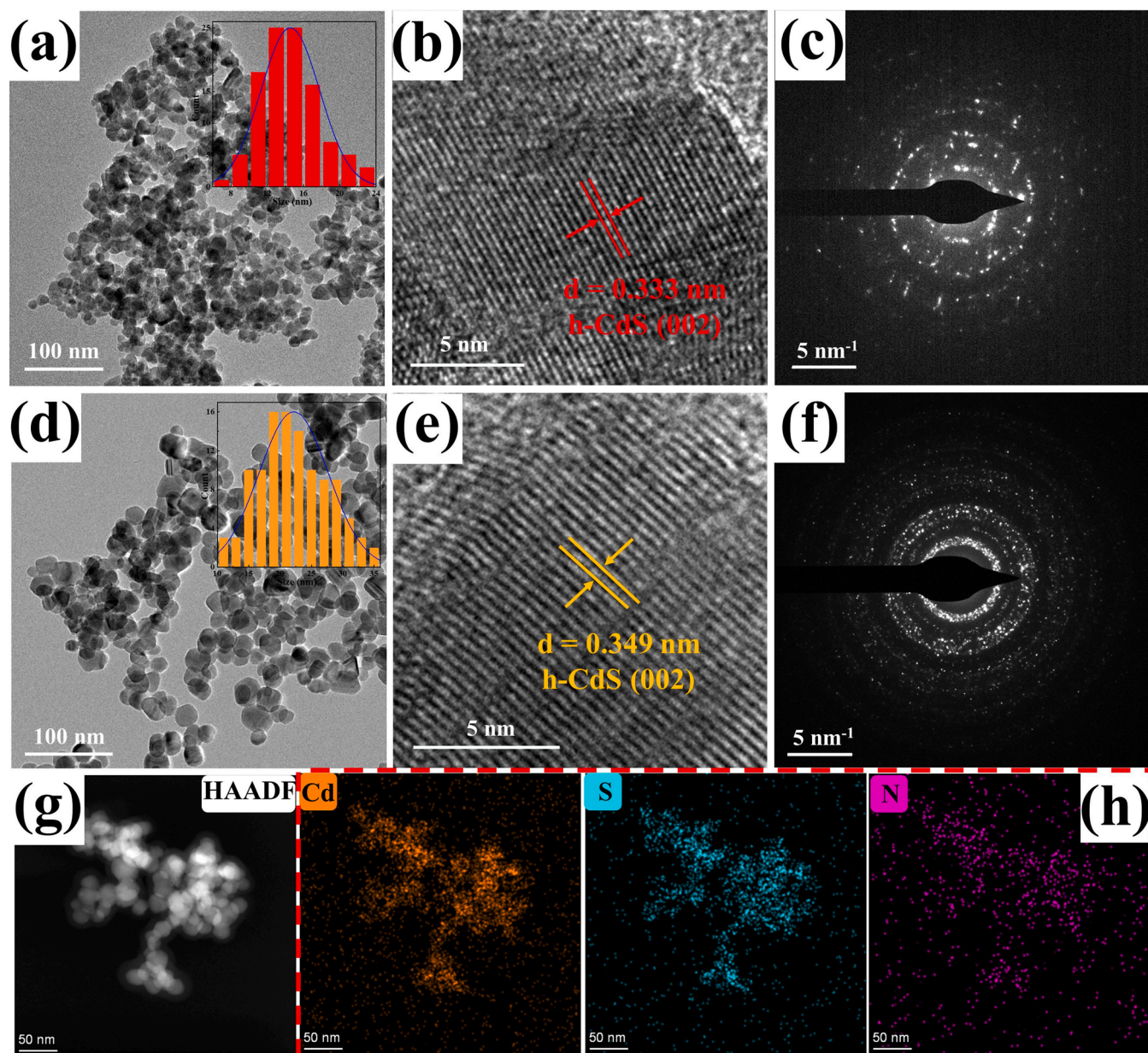
Fig. 2. TEM, HRTEM images and SAED patterns of CdS (a–c) and $N_{0.2}$-CdS (d–f). (g) HAADF image and (h) EDX mappings of $N_{0.2}$-CdS. The insets of panel (a) and (b) are corresponding particle size distributions.

2.2. Photocatalytic HER studies

HER photoactivities were evaluated on a closed gas circulation test system (PerfectLight, LabSolar-IIIAG, CN). Typically, 10 mg catalyst was uniformly dispersed in 50 mL DI water containing 15 vol% triethanolamine (TEOA, A.R.), then the suspension was transferred into a quartz reactor equipped a 300 W Xenon lamp (PLS-SXE 300, 1475 μW·cm^{-2}, CN). The temperature was maintained at 5 °C through a circulating cooling system. The H_2 was detected on a gas chromatograph (GC7900, TianM, CN) by using high purity N_2 as carrier gas.

2.3. Photo-electrochemical measurements

Photo-electrochemical properties were measured on an electrochemical workstation (CHI 660E, CN) with a standard three-electrode system consisted of Ag/AgCl electrode (reference electrode), Pt electrode (counter electrode) and ITO glass ($15 \times 15 \times 1$ mm^3) coated by sample (working electrode), and 0.5 M Na_2SO_4 aqueous solution was used as electrolyte. The detailed operation parameters are shown as Supplementary Material, and the potentials were subsequently converted to reversible hydrogen electrode (RHE) potentials according to the equation shown as below [23].

$$E_{RHE} = E_{Ag/AgCl} + 0.197 + 0.059 \text{ pH} \qquad (1)$$

3. Results and discussion

Here, $Na_2S\cdot9\,H_2O$ and $Cd(Ac)_2\cdot2\,H_2O$ were chosen as precursors, urea was used as doping precursor, and a series of N doped CdS nanocatalysts with different dosages of N heteroatoms were synthesized via a two-step approach. The SSL-induced HER photoactivities of as-synthesized nanocatalysts were evaluated, and the $N_{0.2}$-CdS nanocatalyst was determined as the optimum catalyst (Fig. S1). Thereby, the
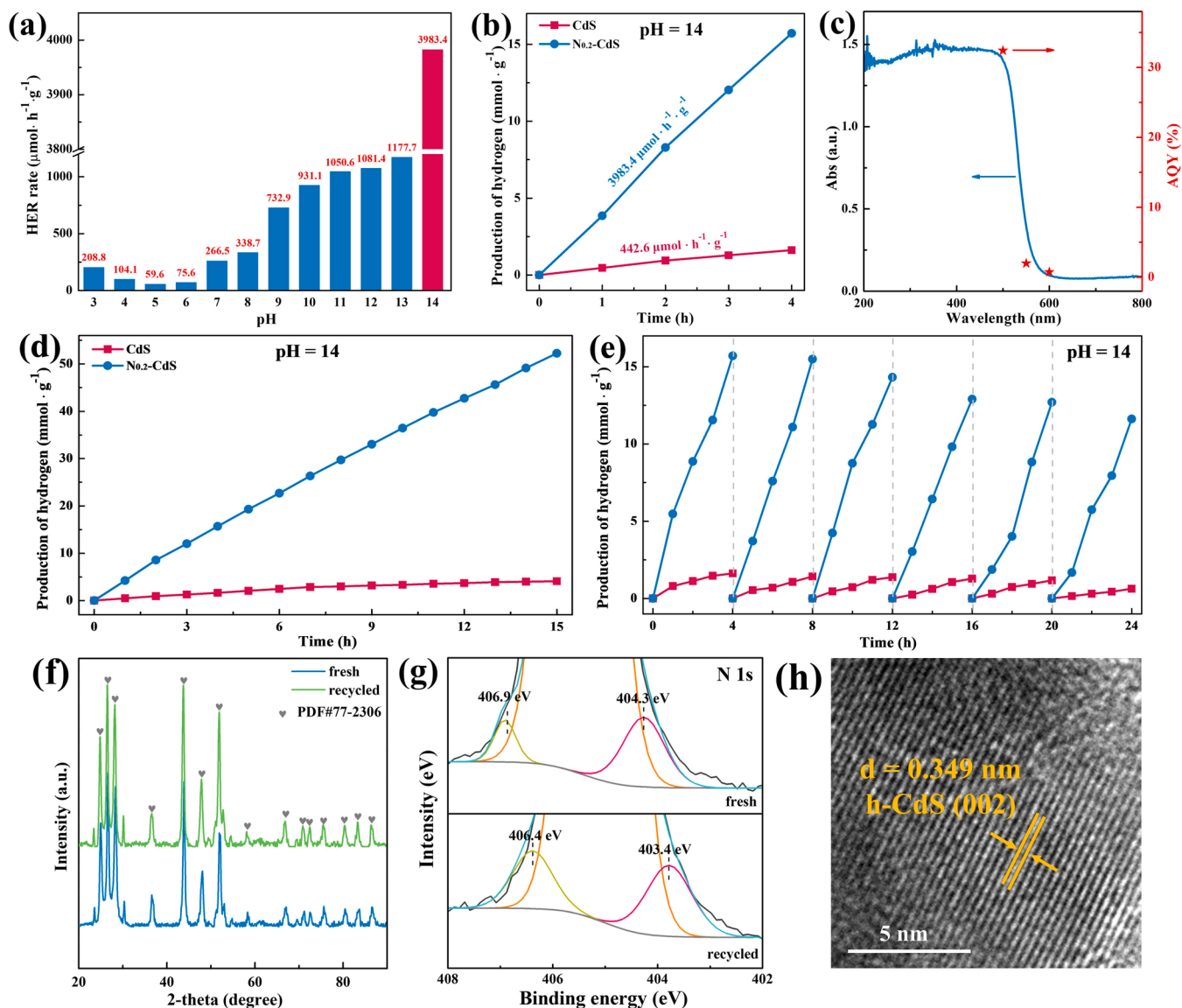
Fig. 3. (a) pH value optimization of HER system (pH = 3–14), (b) SSL-induced HER kinetics, (d) HER durability kinetics and (e) HER recycling kinetics of CdS and $N_{0.2}$-CdS. (c) AQYs of $N_{0.2}$-CdS (500, 550, 600 nm). (f) XRD patterns, (g) N 1s XPS core-level spectra of fresh and recovered $N_{0.2}$-CdS. (h) HRTEM images of recovered $N_{0.2}$-CdS.

optimum nanocatalyst was characterized by various techniques.

3.1. Microstructure and morphology

X-ray diffractometer (XRD) was performed to study the crystal structure of the samples. As shown in Fig. 1(a), both the diffraction peaks of bare CdS and $N_{0.2}$-CdS index well to hexagonal phase CdS (h-CdS, PDF#77-2306) [24], and the impurity peaks are not appeared after N doping. However, three strong diffraction peaks assigned to (100), (002) and (101) crystal planes of h-CdS appear slight blue-shifts, which attributes to that the N heteroatoms enter the lattice of h-CdS. Raman spectroscopy was also applied to characterize the samples. As presented in Fig. 1(b), the peak intensity ratio of 1-LO mode and 2-LO mode for $N_{0.2}$-CdS (I_1/I_2 = 2.18) is greater than that of bare CdS (I_1/I_2 = 1.67), which is caused by the coordination interaction between N atoms and Cd atoms. Then, X-ray photoelectron spectroscopy (XPS) was adopted to study the composition and chemical state of the samples. Due to the similar binding energy region of Cd $3d_{5/2}$ orbital and N 1 s chemical state, it is hard to clearly identify two elements from the survey spectra in Fig. S2. However, the N 1 s core-level spectrum in Fig. 1(c) clearly

presents the characteristics of N 1s chemical state, and the peaks located at 406.9 eV and 404.4 eV ascribe to the oxidative nitrogen species [25]. The Fourier transform infrared (FTIR) spectra in Fig. S4 shows that the $N_{0.2}$-CdS appears two strong absorption peaks at 854 cm^{-1} and 619 cm^{-1} compared with bare CdS, which ascribes to the Cd-N coordination interaction. Also, the slight shifts of Cd 3d (0.1 eV, Fig. 1(d)) and S 2p (0.2 eV, Fig. 1(e)) characteristic peaks to higher binding energy can be observed from their core-level spectra, which attributes to the influence of Cd–N coordination interaction and provides the evidence for Raman conclusion [26].

The microstructures and morphologies of bare CdS and $N_{0.2}$-CdS were observed through transmission electron microscope (TEM) technique. Fig. 2(a–d) show that both bare CdS and $N_{0.2}$-CdS appear near-spherical micromorphology, and their insets reveal that the average particle size of $N_{0.2}$-CdS (~22.1 nm) is larger than that of bare CdS (~14.5 nm), which suggests that N doping benefits to the grain growth of CdS. The widened half-peak width in XRD patterns (Fig. 1(a)) can also support this conclusion well. Moreover, HRTEM images in Fig. 2(b) and (e) show that the lattice distance of $N_{0.2}$-CdS (d = 0.349 nm) is wider than that of bare CdS (d = 0.333 nm), which provides powerful evidence

Table 1
HER performance contrast between this study and reported literatures.

No.	Catalysts	$^a C_{solid}$ (g/L)	Sacrificial agent	Vs. CdS (times)	Light source	AQY (%)	Refs.
1	WO_3/CdS	0.25	Lactic acid	4.12	300 W Xe lamp	13.10 (405 nm)	[29]
2	$g\text{-}C_3N_4/CdS$	0.42	Lactic acid	5	300 W Xe lamp	2.79 (420 nm)	[30]
3	$NiS\text{-}Mo_2C/CdS$	0.15	$Na_2S + Na_2SO_3$	7.83	300 W Xe lamp	12.20 (420 nm)	[31]
4	CdS/NiAl LDH	0.33	$Na_2S + Na_2SO_3$	6.31	5 W LED light	/	[32]
5	$Ti_3C_2T_x/CdS$	0.25	Lactic acid	2	300 W Xe lamp	10.20 (450 nm)	[33]
6	CdS@Mn-ZIF-67	1	$Na_2S + Na_2SO_3$	5	300 W Xe lamp	10.10 (420 nm)	[34]
7	$H\text{-}Co_3O_4@CdS$	0.4	TEOA	7.3	300 W Xe lamp	32.21 (420 nm)	[35]
8	CdS/Ti_3C_2 MXene	0.2	Lactic acid	7	300 W Xe lamp	35.6 (420 nm)	[36]
9	CdS/TiO_2	/	Methanol	4	300 W Xe lamp	10.14	[37]
10	NC@Co-NCT/CdS	0.2	Lactic acid	5.8	300 W Xe lamp	17.20 (500 nm)	[38]
11	Mn-ZIF-67/CdS	0.4	$Na_2S + Na_2SO_3$	1.4	300 W Xe lamp	3.20 (400 nm)	[39]
12	Ru/CdS/Halloysite	0.2	$Na_2S + Na_2SO_3$	7.2	30 W LED light	9.30 (450 nm)	[40]
13	CdS/C_3N_4	0.06	$Na_2S + Na_2SO_3$	3.83	300 W Xe lamp	6.86 (420 nm)	[41]
14	BPQDs/CdS	0.5	Lactic acid	5.5	100 W LED light	/	[42]
15	**$N_{0.2}\text{-}CdS$**	**0.2**	**TEOA**	**9**	**300 W Xe lamp**	**32.41 (500 nm)**	**This work**

$^a C_{solid}$ is the solid content of photoreaction system.

for entrance of N heteroatoms to the lattice of CdS. The selected area electron diffraction (SAED) patterns in Fig. 2(c) and (f) reveal that N-doping increases the crystallinity of CdS [27], and it is consistent with the XRD results, which can be attributed to the stronger coordination ability of N heteroatoms. Additionally, high-angle annular dark field (HAADF) image in Fig. 2(g) reveals the uniform phase state, and energy dispersive X-ray (EDX) mappings in Fig. 2(h) also display the uniform distribution of N element in body structure of CdS NPs, which is very benefited to the formation of synergetic HSC interaction between Cd atoms and N atoms.

3.2. SSL-induced HER performance

The photoactivities of nanocatalysts were evaluated according to their HER performances at presence of TEOA under SSL-irradiation. As shown in Fig. S1, N doping effectively improves the HER activity of bare CdS NPs, and the $N_{0.2}$-CdS nanocatalyst is determined as the optimum catalyst for its highest HER rate (1050.6 $\mu mol \cdot h^{-1} \cdot g^{-1}$) during 4 h of SSL-irradiation, then its HER rate is further increased to 3983.4 $\mu mol \cdot h^{-1} \cdot g^{-1}$ by optimizing pH value of reaction system (optimum pH = 14, Fig. 3(a)) due to the proper H^+ concentration and effective Coulomb drag of photogenerated holes [28], which raises to about 9-fold greater than that of bare CdS NPs (442.6 $\mu mol \cdot h^{-1} \cdot g^{-1}$). When excess N heteroatoms enter the body structure of CdS NPs, the synergetic HSC interaction is negatively affected due to the breaking of crystal structure of CdS, leading to the decreased HER activity. As displayed in Fig. S3, when increasing the dosage of N heteroatom, the peak intensity of XRD pattern decreases gradually, which supports above conclusion well. Furthermore, Fig. 3(c) displays the AQYs of $N_{0.2}$-CdS nanocatalyst for H_2 production under different fixed wavelengths of photoirradiation (500 nm, 550 nm, 600 nm), and about 32.4% of AQY can be achieved at the wavelength of 500 nm, which is much higher than most reported data of CdS-based photocatalysts for H_2 production (Table 1) [29–42]. The high AQY suggests high-efficient utilization of photoexcited carriers, which is attributed to the promoted body carriers migration due to the synergetic influence of HSC interaction.

Then, the photostability of $N_{0.2}$-CdS nanocatalyst was examined. The HER activity of bare CdS NPs presents obvious attenuation in a short irradiated-time (2–3 h, Fig. S5), but $N_{0.2}$-CdS nanocatalyst holds a very stale and highly improved HER activity in a long irradiated-time (15 h, Fig. 3(d)). Moreover, Fig. 3(e) shows that the HER activity of $N_{0.2}$-CdS nanocatalyst presents slower decline as cycle time increases. The recovered $N_{0.2}$-CdS nanocatalyst was characterized by XRD and XPS techniques. Fig. 3(f–g) show that the recovered $N_{0.2}$-CdS nanocatalyst appears very similar crystal and chemical state characteristics with the fresh sample, and only slight peak shifts to lower binding energy can be observed in Fig. 3(g). Meanwhile, the HRTEM image of recovered $N_{0.2}$-CdS nanocatalyst displays unchanged lattice feature compared with fresh sample (Fig. 3(h)). According to above results, it can be confirmed that the photocorrosion of bare CdS can be effectively restained by N doping, so the $N_{0.2}$-CdS nanocatalyst not only possesses remarkably enhanced HER activity but also excellent photostability even suffering long-term irradiation.

3.3. Photo-electrochemical properties and band structure

UV–vis absorption spectra were measured to study the light-harvesting and optical-response properties of bare CdS and $N_{0.2}$-CdS nanocatalysts. As shown in Fig. 4(a), after N doping, the absorption edge of CdS appears slight blue-shift (578 nm → 568 nm), and the corresponding bandgap (E_g) broadens to 2.29 eV from original 2.27 eV, which is very different from the commonly reported results [43]. However, the doped sample still show excellent light-harvesting and response characteristics in visible-light range. Moreover, the separation and recombination behaviors of photoexcited carriers were investigated by electrochemical and photoluminescence (PL) techniques. The photoinduced linear sweep voltammetry (LSV) curves in Fig. 4(d) show that the $N_{0.2}$-CdS nanocatalyst appears highly enhanced photocurrent signals than that of bare CdS in a wide range of initial potentials (-0.7 to -0.3 V), and same result is obtained at transient photocurrent response curves recorded at the initial potential of -0.2 V (Fig. 4(e)). Considering the broadened E_g of $N_{0.2}$-CdS nanocatalyst, it reveals that N doping
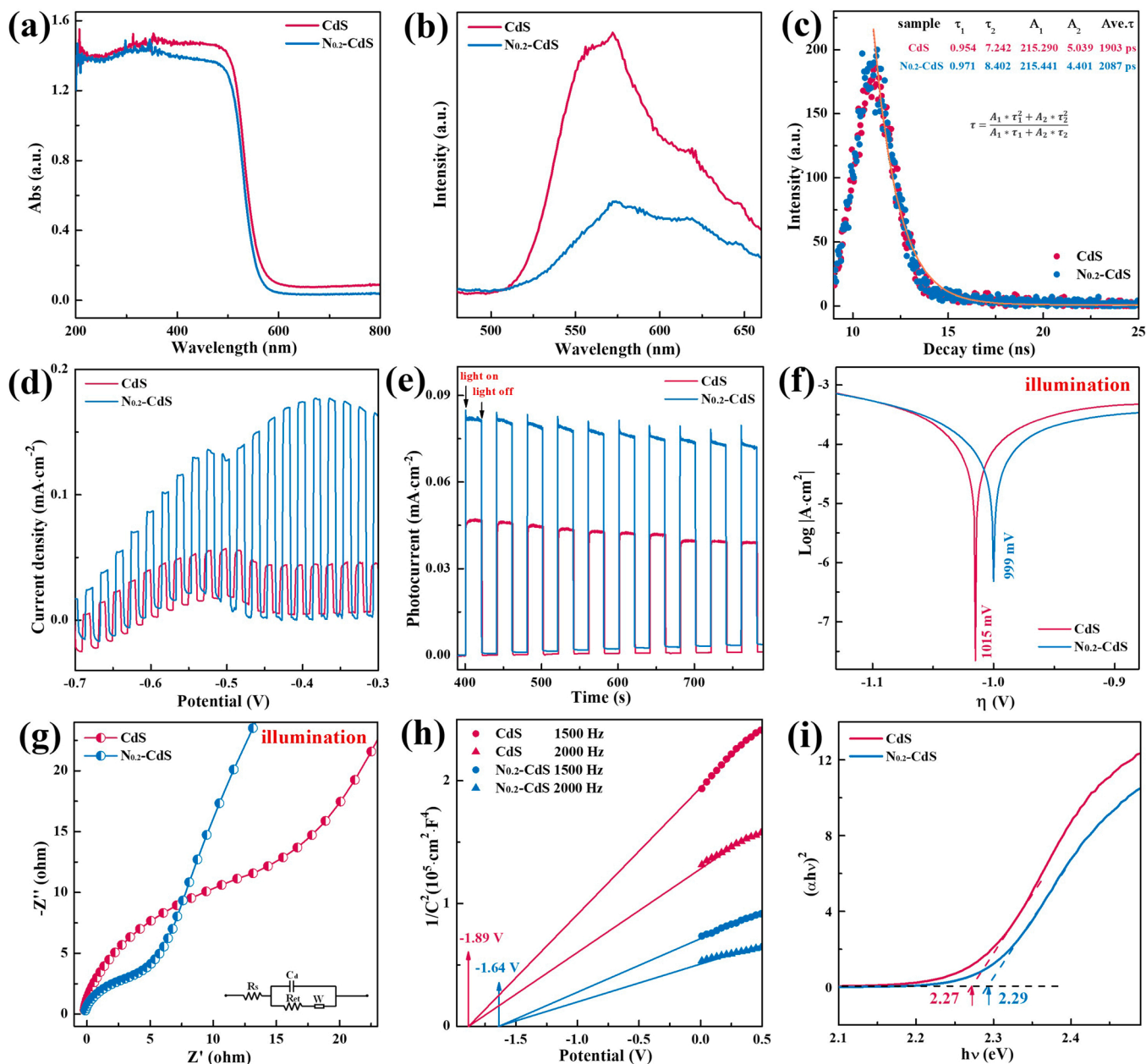
Fig. 4. (a) UV–vis absorption spectra, (b) PL spectra, (c) TRPL spectra, (d) LSV curves, (e) transient photocurrent responses, (f) Tafel curves, (g) EIS plots, (h) Mott-Schottky plots (1500 Hz and 2000 Hz) and (i) $(\alpha h\nu)^2 \sim h\nu$ patterns of CdS and $N_{0.2}$-CdS. All the LSV, Tafel and EIS data were tested under illumination.

effectively hinders the recombination behavior of photoexcited carriers in CdS body structure and results in remarkably increased photocurrent intensity (~2 times). As shown in Fig. 4(b–c), at the same excitation wavelength of 380 nm, $N_{0.2}$-CdS nanocatalyst displays obviously weakened PL intensity and longer photoexcited carriers retention time (2087 ps) than bare CdS (1903 ps), which provides the direct evidence for restrained recombination behavior of photoexcited carriers, so more opportunities are ensured to participate in H_2 production. This attributes to the promoted carriers mobility for synergetic effect of N heteroatom sites in body structure of CdS. Additionally, Tafel curves in Fig. 4(f) show that $N_{0.2}$-CdS nanocatalyst appears smaller polarized overpotential (999 mV) than that of bare CdS (1015 mV) at the same electrochemical test parameters, suggesting higher reaction possibility for H_2 production. Besides, electrochemical impedance spectroscopy (EIS) was recorded under photoinduction to analyze the interfacial conductivity. As shown in Fig. 4(g), a smaller Nyquist semicircle is presented by $N_{0.2}$-CdS nanocatalyst compared with bare CdS, which indicates that N

doping remarkably promotes body carriers migration of CdS. This is the main reason for restrained recombination behavior of photoexcited carriers. Thereby, the promoted separation and prolonged retention time of photoexcited carriers are the internal driving force for improving the HER activity of $N_{0.2}$-CdS nanocatalyst.

To understand the band structure of $N_{0.2}$-CdS nanocatalyst, Flat-band potentials (E_{fb}) of bare CdS and $N_{0.2}$-CdS were determined according to their Mott-Schottky plots tested at different frequencies (1.5 and 2.0 kHz). As labeled in Fig. 4(h), the E_{fb} of bare CdS and $N_{0.2}$-CdS are −1.89 $V_{Ag/AgCl}$/−1.28 V_{RHE} and −1.64 $V_{Ag/AgCl}$/−1.03 V_{RHE}, respectively [44]. Because the n-type feature of CdS semiconductor, the E_{CB} of bare CdS and $N_{0.2}$-CdS can be confirmed as −1.48 V_{RHE} and −1.23 V_{RHE} according to the reported calculation method [45]. Based on the E_g of bare CdS and $N_{0.2}$-CdS in Fig. 4(i), their valence band maximums (E_{VB}) can be calculated to be 0.79 V_{RHE} and 1.06 V_{RHE} according to the equation of $E_{VB} = E_g + E_{CB}$.[46] Combining the XPS-VBs spectra in Fig. 1(f), Fermi level positions (E_f) of CdS and $N_{0.2}$-CdS can be confirmed
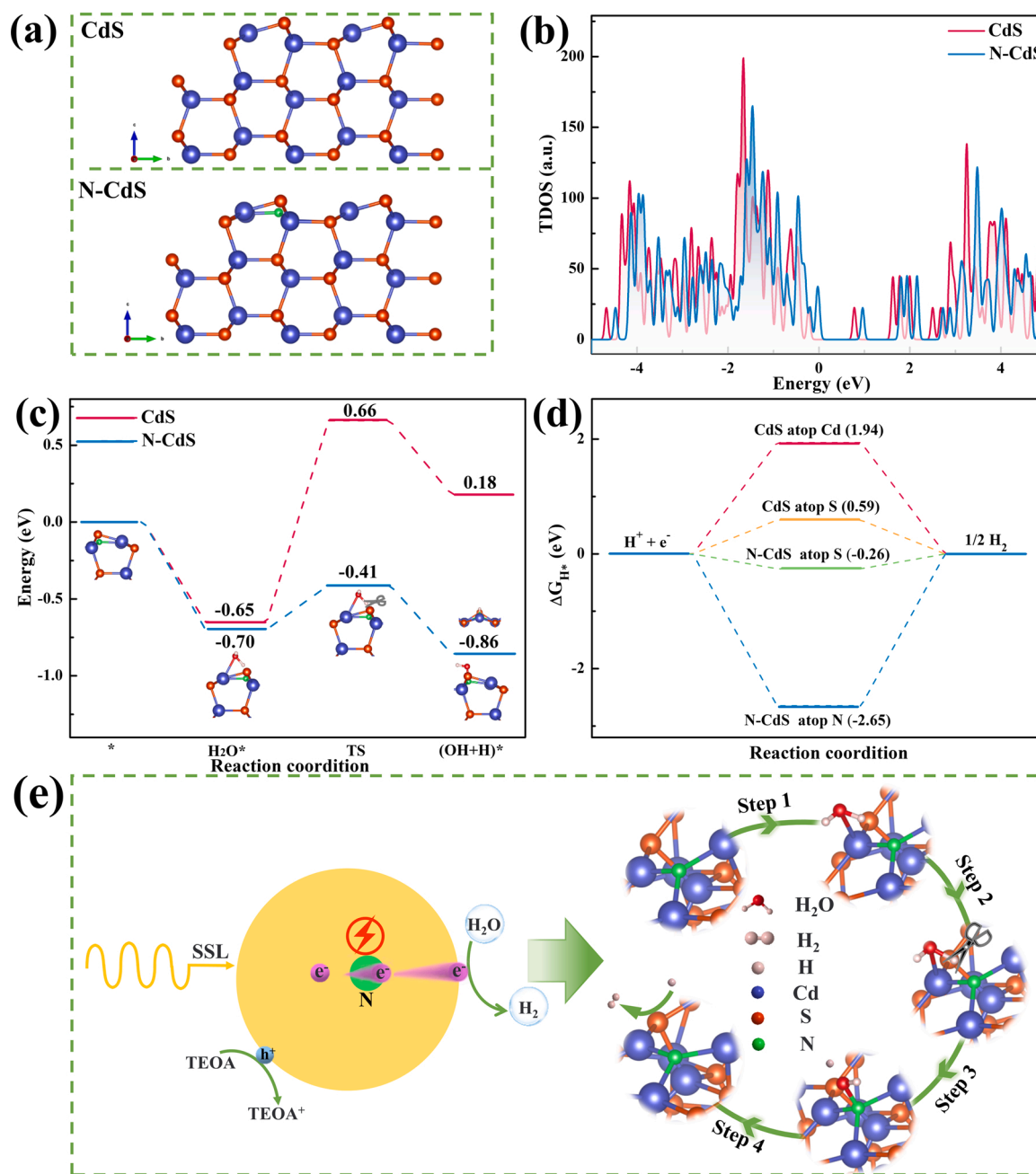
Fig. 5. (a) Optimized conformation models, (b) TDOS, (c) energy barriers of water dissociation and (d) ΔG_{H*} of CdS and $N_{0.2}$-CdS. (e) Synergetic promotion of body carriers migration and SSL-induced HER mechanism on $N_{0.2}$-CdS nanocatalyst.

to be -0.67 V_{RHE} and -0.76 V_{RHE}. Obviously, although the CB position of $N_{0.2}$-CdS is more positive than bare CdS, its E_f is more negative, which is the internal reason for higher photoinduced reducing capacity.

3.4. DFT calculations and HER mechanism

DFT calculations were adopted to further investigate the HSC interaction in body structure of $N_{0.2}$-CdS nanocatalyst and discuss its HER mechanism based on the first principles. Fig. 5(a) shows the optimized conformation models of CdS and N-CdS based on the (100) crystal plane of h-CdS, and the Cd-N-Cd coordination interaction appears in the optimized N-CdS model. The total density of states (TDOS) in Fig. 5(b) show that the N-CdS model possesses decreased electron density than CdS model, which attributes to the equalization of electron density for coordination interaction between Cd atom and N heteroatom and

provides theoretical evidence for promoted carriers migration. Meanwhile, the partial density of states (PDOS) in Fig. S6 show that the p orbital of N heteroatom (Fig. S6(c)) appears obvious electron density overlap with d orbital of Cd atom (Fig. S6(a)), indicating the possibility of hybridization between N heteroatom and Cd atom. It provides the reliable evidence for the formation of Cd-N-Cd coordination interaction. Furthermore, the energy barriers for water dissociation and H_2 generation were calculated. As displayed in Fig. 5(c), all the H_2O molecule adsorption (H_2O*), transition state (TS) and H_2O molecule dissociation processes present remarkably reduced energy barriers on N-CdS model compared with CdS model, indicating that the formation of Cd-N-Cd coordination interaction thermodynamically enhance H_2O molecule adsorption and accelerate its dissociation. Fig. 5(d) shows the corresponding energy barrier diagram of H_2 generation, and a preferred H_2 generation should possess a $|\Delta G_{H*}|$ value close to zero. Notably, N

heteroatom site displays much larger $|\Delta G_{H*}|$ value (2.65 eV) than other sites, and S site displays smallest $|\Delta G_{H*}|$ value (0.26 eV), which powerfully demonstrates that S atoms are the main active sites for H_2 generation. Moreover, the $|\Delta G_{H*}|$ value of S sites decreases obviously from original 0.59 eV after N doping, suggesting remarkable promotion of H_2 generation on S sites owing to the synergetic HSC interaction.

Based on the results of DFT calculations, the HER mechanism on $N_{0.2}$-CdS nanocatalyst can be illustrated as Fig. 5(e). Briefly, the adsorbed H_2O molecules are cracked to form H* intermediates and OH⁻ ions on Cd sites. Then, H* intermediates accept electrons from S sites to form H_2 molecules. The oxidizing half-reaction (OH⁻ + h⁺ → O_2 + H_2O) was restrained by adding sacrificial agent (TEOA) to this reaction system. Owing to the dramatically decreased energy barriers of water cracking and H_2 generation on $N_{0.2}$-CdS nanocatalyst, this improved nanocatalyst possesses highly improved HER activity than bare CdS. Meanwhile, due to the synergetic promotion of body carriers migration by HSC interaction, their recombination behavior can be effectively restrained, thereby high quantum yield can be achieved for high-efficient utilization of photoexcited carriers.

4. Conclusion

Fast photoexcited carriers recombination and severe photocorrosion of CdS NPs inevitably result in low carriers utilization, leading to undesirable photocatalytic performance and poor durability. To address the issues, N heteroatoms were introduced into the lattice of h-CdS NPs to synthesize the N-CdS nanocatalyst via a wet chemical precipitation coupled with a hydrothermal process. Due to the synergetic promotion of body carriers migration by HSC interaction, the recombination behavior of photoexcited carriers was effectively hampered, resulting obviously increased photocurrent density (∼2 times) and significantly accelerated photoexcited carriers utilization. Thereby, about 32.41% of AQY (500 nm) was achieved by the optimized $N_{0.2}$-CdS nanocatalyst. Under SSL-irradiation, about 3983.4 $\mu mol \cdot h^{-1} \cdot g^{-1}$ of HER rate with excellent photostability was achieved by this improved nanocatalyst at absence of cocatalyst, which is about 9-fold greater than that of bare CdS NPs. DFT calculations proved that the obviously reduced energy barrier of water splitting on Cd sites and $|\Delta G_{H*}|$ value of H_2 generation on S sites thermodynamically accelerated the H_2 generation due to the synergetic HSC interaction. This study provides a simple and green strategy for gaining highly stable CdS photocatalyst with improved HER photoactivity.

CRediT authorship contribution statement

No conflict of interest exits in the submission of this manuscript, and manuscript is approved by all authors for publication, **Wei Li**: Data curation, Project administration, Resources, Methodology, Supervision, Validation, Writing – original draft, Writing – review & editing. **Fei Wang**: Investigation, Writing – original draft, Writing – review & editing. **Xiao-yun Liu**: Investigation. **Yan-yan Dang**: Investigation. **Jia-yuan Li**: Investigation. **Teng-hao Ma**: Investigation. **Chuan-yi Wang**: Resources, Methodology, Supervision, Validation.

Declaration of Competing Interest

The authors declare no conflict of interest.

Acknowledgements

Appendix A. Supporting information

Supplementary data associated with this article can be found in the online version at doi:10.1016/j.apcatb.2022.121470.

References

[1] a) H. Nishiyama, T. Yamada, M. Nakabayashi, Y. Maehara, M. Yamaguchi, Y. Kuromiya, Y. Nagatsuma, H. Tokudome, S. Akiyama, T. Watanabe, R. Narushima, S. Okunaka, N. Shibata, T. Takata, T. Hisatomi, K. Domen, Photocatalytic solar hydrogen production from water on a 100-m2 scale, Nature 598 (2021) 304–307;
b) Q. Wang, J. Warnan, S. Rodríguez-Jiménez, J.J. Leung, S. Kalathil, V. Andrei, K. Domen, E. Reisner, Molecularly engineered photocatalyst sheet for scalable solar formate production from carbon dioxide and water, Nat. Energy 5 (2020) 703–710;
c) X. Yin, R. Yang, G. Tan, S. Fan, Terrestrial radiative cooling: Using the cold universe as a renewable and sustainable energy source, Science 370 (2020) 786–791.
[2] a) N.-N. Vu, S. Kaliaguine, T.-O. Do, Critical aspects and recent advances in structural engineering of photocatalysts for sunlight-driven photocatalytic reduction of CO2 into fuels, Adv. Funct. Mater. 29 (2019) 1901825;
b) J. Jiang, D. Duan, J. Ma, Y. Jiang, R. Long, C. Gao, Y. Xiong, Van der waals heterostructures by single cobalt sites-anchored graphene and g-C3N4 nanosheets for photocatalytic syngas production with tunable CO/H2 ratio, Appl. Catal. B Environ. 295 (2021), 120261.
[3] S. Gao, B. Gu, X. Jiao, Y. Sun, X. Zu, F. Yang, W. Zhu, C. Wang, Z. Feng, B. Ye, Y. Xie, Highly efficient and exceptionally durable CO2 photoreduction to methanol over freestanding defective single-unit-cell bismuth vanadate layers, J. Am. Chem. Soc. 139 (2017) 3438–3445.
[4] a) Y. Chai, Y. Chen, J. Shen, M. Ni, B. Wang, D. Li, Z. Zhang, X. Wang, Distortion of the coordination structure and high symmetry of the crystal structure in In4SnS8 microflowers for enhancing visible-light photocatalytic CO2 reduction, ACS Catal. 11 (2021) 11029–11039;
b) Y. Yu, X. Dong, P. Chen, Q. Geng, H. Wang, J. Li, Y. Zhou, F. Dong, Synergistic effect of Cu single atoms and Au-Cu alloy nanoparticles on TiO2 for efficient CO2 photoreduction, ACS Nano 15 (2021) 14453–14464.
[5] a) S. Sorcar, Y. Hwang, J. Lee, H. Kim, K.M. Grimes, C.A. Grimes, J.-W. Jung, C.-H. Cho, T. Majima, M.R. Hoffmannd, S.-I. In, Platinum- and CuOx -decorated TiO2 photocatalyst for oxidative coupling of methane to C2 hydrocarbons in a flow reactor, Energy Environ. Sci. 12 (2019) 2685–2696;
b) X. Li, J. Xie, H. Rao, C. Wang, J. Tang, Angew. Chem. Int. Ed 59 (2020) 19702–19707.
[6] a) L. Lin, Z. Lin, J. Zhang, X. Cai, W. Lin, Z. Yu, X. Wang, Molecular-level insights on the reactive facet of carbon nitride single crystals photocatalysing overall water splitting, Nat. Catal. 3 (2020) 649–655;
b) S. Cao, X. Wu, Y. Chen, S. Qiu, X. Liu, C. Sun, L. Piao, Water as a cocatalyst for photocatalytic H2 production from formic acid, Nano Today 35 (2020), 100968.
[7] a) X. Wang, X. Wang, J. Huang, S. Li, A. Meng, Z. Li, Interfacial chemical bond and internal electric field modulated Z-scheme Sv-ZnIn2S4/MoSe2 photocatalyst for efficient hydrogen evolution, Nat. Commun. 12 (2021) 4112;
b) W. Jiang, Y. Zhao, X. Zong, H. Nie, L. Niu, L. An, D. Qu, X. Wang, Z. Kang, Z. Sun, Photocatalyst for high-performance H2 production: Ga-doped polymeric carbon nitride, Angew. Chem. Int. Ed. 133 (2021) 6189–6194;
c) L. Jiao, Y. Dong, X. Xin, L. Qin, H. Lv, Facile integration of Ni-substituted polyoxometalate catalysts into mesoporous light-responsive metal-organic framework for effective photogeneration of hydrogen, Appl. Catal. B Environ. 291 (2021), 120091.
[8] a) J. Xiao, J.M. Vequizo, T. Hisatomi, J. Rabeah, M. Nakabayashi, Z. Wang, Q. Xiao, H. Li, Z. Pan, M. Krause, N. Yin, G. Smith, N. Shibata, A. Brückner, A. Yamakata, T. Takata, K. Domen, Simultaneously tuning the defects and surface properties of Ta3N5 nanoparticles by Mg-Zr codoping for significantly accelerated photocatalytic H2 evolution, J. Am. Chem. Soc. 143 (2021) 10059–10064;
b) C. Cheng, B. He, J. Fan, B. Cheng, S. Cao, J. Yu, An inorganic/organic s-scheme heterojunction h2-production photocatalyst and its charge transfer mechanism, Adv. Mater. 33 (2021) 2100317.
[9] a) C. Orrison, J.R. Meeder, B. Zhang, J. Puthenpurayil, M.B. Hall, M. Nippe, D. H. Son, Efficient redox-neutral photocatalytic formate to carbon monoxide conversion enabled by long-range hot electron transfer from Mn-doped quantum dots, J. Am. Chem. Soc. 143 (2021) 10292–10300;
b) W. Jiang, Y. Zhao, X. Zong, H. Nie, L. Niu, L. An, D. Qu, X. Wang, Z. Kang, Z. Sun, Photocatalyst for high-performance H2 production: Ga-doped polymeric carbon nitride, Angew. Chem. Int. Ed. 60 (2021) 6124–6129.
[10] a) M.A. Lange, I. Khan, P. Opitz, J. Hartmann, M. Ashraf, A. Qurashi, L. Prädel, M. Panthöfer, A. Cossmer, J. Pfeifer, F. Simon, M. Au, B. Meermann, M. Mondeshki, M.N. Tahir, W. Tremel, A generalized method for high-speed fluorination of metal oxides by spark plasma sintering yields Ta3O7F and TaO2F with high photocatalytic activity for oxygen evolution from water, Adv. Mater. 33 (2021) 2007434;
b) F. Yu, C. Wang, Y. Li, H. Ma, R. Wang, Y. Liu, N. Suzuki, C. Terashima, B. Ohtani, T. Ochiai, A. Fujishima, X. Zhang, Enhanced solar photothermal catalysis over solution plasma activated TiO2, Adv. Sci. 7 (2020) 2000204.
[11] a) Y.-X. Tan, Z.-M. Chai, B.-H. Wang, S. Tian, X.-X. Deng, Z.-J. Bai, L. Chen, S. Shen, J.-K. Guo, M.-Q. Cai, C.-T. Au, S.-F. Yin, Boosted photocatalytic oxidation of toluene into benzaldehyde on CdIn2S4-CdS: synergetic effect of compact

heterojunction and S-vacancy, ACS Catal. 11 (2021) 2492–2503;
b) X. Jin, Y. Fang, T. Salim, M. Feng, Z. Yuan, S. Hadke, T.C. Sum, L.H. Wong, Controllable solution-phase epitaxial growth of Q1D Sb2(S,Se)3/CdS heterojunction solar cell with 9.2% efficiency, Adv. Mater. 33 (2021) 2104346.

[12] a) Q. Dong, M. Li, M. Sun, F. Si, Q. Gao, X. Cai, Y. Xu, T. Yuan, S. Zhang, F. Peng, Y. Fang, S. Yang, Phase-controllable growth NixPy modified CdS@Ni3S2 electrodes for efficient electrocatalytic and enhanced photoassisted electrocatalytic overall water splitting, Small Methods 5 (2021) 2100878;
b) L.C. Spangler, J.P. Cline, J.D. Sakizadeh, C.J. Kielyab, S. McIntosh, Enzymatic synthesis of supported CdS quantum dot/reduced graphene oxide photocatalysts, Green Chem. 21 (2019) 4046–2104054.

[13] a) T. Liu, P. Diao, Z. Lin, H. Wang, Sulfur and selenium doped nickel chalcogenides as efficient and stable electrocatalysts for hydrogen evolution reaction: The importance of the dopant atoms in and beneath the surface, Nano Energy 74 (2020), 104787;
b) S. Zhang, Z. Zhang, Y. Si, B. Li, F. Deng, L. Yang, X. Liu, W. Dai, S. Luo, Gradient hydrogen migration modulated with self-adapting S vacancy in copper-doped ZnIn2S4 nanosheet for photocatalytic hydrogen evolution, ACS Nano 15 (2021) 15238–15248;
c) H. Bergeron, D. Lebedev, M.C. Hersam, Polymorphism in post-dichalcogenide two-dimensional materials, Chem. Rev. 121 (2021) 2713–2775.

[14] a) W. Li, X. Chu, F. Wang, Y. Dang, X. Liu, T. Ma, J. Li, C. Wang, Pd single-atom decorated CdS nanocatalyst for highly efficient overall water splitting under simulated solar light, Appl. Catal. B Environ. 304 (2022) 121000;
b) Y.-T. Liu, M.-Y. Lu, T.-P. Perng, L.-J. Chen, Plasmonic enhancement of hydrogen production by water splitting with CdS nanowires protected by metallic TiN overlayers as highly efficient photocatalysts, Nano Energy 89 (2021), 106407;
c) X.S. Wang, Q. Ma, F. Wang, X. Chu, X. Wang, C. Wang, CdS@h-BN heterointerface construction on reduced graphene oxide nanosheets for hydrogen production, Appl. Catal. B Environ. 284 (2021), 119688;
d) J. He, L. Hu, C. Shao, S. Jiang, C. Sun, S. Song, Photocatalytic H2O overall splitting into h2bubbles by single atomic sulfur vacancy CdS with spin polarization electric field, ACS Nano 15 (2021) 18006–18013.

[15] a) W. Li, X. Liu, X. Chu, F. Wang, Y. Dang, T. Ma, J. Lia, C. Wang, Fast Cr(vi) wastewater remediation on a BixOy/CdS heterostructure under simulated solar light induction, Environ. Sci. Nano 8 (2021) 3655–3664;
b) H.-N. Wang, Y.-H. Zou, Y.-M. Fu, X. Meng, L. Xue, H.-X. Suna, Z.-M. Su, Integration of zirconium-based metal-organic framework with CdS for enhanced photocatalytic conversion of CO2 to CO, Nanoscale 13 (2021) 16977–16985.

[16] R. Feng, K. Wan, X. Sui, N. Zhao, H. Li, W. Lei, J. Yu, X. Liu, X. Shi, M. Zhai, G. Liu, H. Wang, L. Zheng, M. Liu, Anchoring single Pt atoms and black phosphorene dual co-catalysts on CdS nanospheres to boost visible-light photocatalytic H2 evolution, Nano Today 37 (2021), 101080.

[17] R. Chen, Z.-H. Yan, X.-J. Kong, L.-S. Long, L.-S. Zheng, Integration of lanthanide-transition-metal clusters onto cds surfaces for photocatalytic hydrogen evolution, Angew. Chem. Int. Ed. 57 (2018) 16796–16800.

[18] X. Xiang, B. Zhu, B. Cheng, J. Yu, H. Lv, Enhanced photocatalytic H2-production activity of cds quantum dots using Sn2+as cocatalyst under visible light irradiation, Small 16 (2020), 2001024.

[19] a) M. Guo, G. Ma, Chemical profiling of embelia ribes by ultra-high-performance liquid chromatography quadrupole time-of-flight tandem mass spectrometry and its antioxidant and anti-inflammatory activities in vitro, J. Catal. 391 (2020) 241–246;
b) M. Xia, X. Yan, H. Li, N. Wells, G. Yang, Well-designed efficient charge separation in 2D/2D N doped La2Ti2O7/ZnIn2S4 heterojunction through band structure/morphology regulation synergistic effect, Nano Energy 78 (2020), 105401;
c) J. Cui, Y. Luo, B. Dong, Y. Qi, M. Jia, F. Zhang, C. Li, Investigation on the influence of Sc ions doping on the structure and performance of Ta3N5 photocatalyst for water oxidation under visible light irradiation, Sol. RRL 4 (2020) 1900445.

[20] J.-W. Shi, D. Sun, Y. Zou, D. Ma, C. He, X. Ji, C. Niu, Trap-level-tunable Se doped CdS quantum dots with excellent hydrogen evolution performance without co-catalyst, Chem. Eng. J. 364 (2019) 11–19.

[21] R. Shi, H.-F. Ye, F. Liang, Z. Wang, K. Li, Y. Weng, Z. Lin, W.-F. Fu, C.-M. Che, Y. Chen, Interstitial P-doped CdS with long-lived photogenerated electrons for photocatalytic water splitting without sacrificial agents, Adv. Mater. 30 (2018), 1705941.

[22] M. Zubair, E.M.M. Vanhaecke, I.-H. Svenum, M. Rønning, J. Yang, Core-shell particles of C-doped CdS and graphene: a noble metal-free approach for efficient photocatalytic H2 generation, Green Energy Environ. 5 (2020) 461–472.

[23] P. Bhavani, D.P. Kumar, A.P. Rangappa, Y. Hong, M. Gopannagari, D.A. Reddy, T. K. Kim, Skeletal Cu7S4 nanocages wrapped by few-layered black phosphorus nanosheets as an efficient H2 production photocatalyst, ChemCatChem 13 (2021) 304–312.

[24] H. Huang, Z. Wang, B. Luo, P. Chen, T. Lin, M. Xiao, S. Wang, B. Dai, W. Wang, J. Kou, C. Lu, Z. Xu, L. Wang, Design of twin junction with solid solution interface for efficient photocatalytic H2 production, Nano Energy 69 (2020), 104410.

[25] a) T. Xiong, X. Dong, H. Huang, W. Cen, Y. Zhang, F. Dong, Single precursor mediated-synthesis of Bi semimetal deposited N-doped (BiO)2CO3 superstructures for highly promoted photocatalysis, ACS Sustain. Chem. Eng. 4 (2016) 2969–2979;
b) J.A. Rengifo-Herrera, K. Pierzchała, A. Sienkiewicz, L. Forró, J. Kiwi, C. Pulgarin, Abatement of organics and Escherichia coli by N, S co-doped TiO2

under UV and visible light. Implications of the formation of singlet oxygen (1O2) under visible light, Appl. Catal. B Environ. 88 (2009) 398–406.

[26] C. Lu, L. Yang, B. Yan, L. Sun, P. Zhang, W. Zhang, Z. Sun, Nitrogen-doped Ti3C2MXene: mechanism investigation and electrochemical analysis, Adv. Funct. Mater. 30 (2020), 2000852.

[27] a) M. Jahdi, S.B. Mishra, E.N. Nxumalo, S.D. Mhlanga, A.K. Mishra, Smart pathways for the photocatalytic degradation of sulfamethoxazole drug using F-Pd co-doped TiO2 nanocomposites, Appl. Catal. B Environ. 267 (2020), 118716;
b) S. Luo, H. Lin, Q. Wang, X. Ren, D. Hernández-Pinilla, T. Nagao, Y. Xie, G. Yang, S. Li, H. Song, M. Oshikiri, J. Ye, Triggering water and methanol activation for solar-driven H2 production: interplay of dual active sites over plasmonic ZnCu Alloy, J. Am. Chem. Soc. 143 (2021) 12145–12153.

[28] T. Simon, N. Bouchonville, M.J. Berr, A. Vaneski, A. Adrović, D. Volbers, R. Wyrwich, M. Döblinger, A.S. Susha, A.L. Rogach, F. Jäckel, J.K. Stolarczyk, J. Feldmann, Redox shuttle mechanism enhances photocatalytic H2 generation on Ni-decorated CdS nanorods, Nat. Mater. 13 (2014) 1013–1018.

[29] Y. Lu, Y. Li, Y. Wang, J. Zhang, Two-photon induced NIR active core-shell structured WO3/CdS for enhanced solar light photocatalytic performance, Appl. Catal. B Environ. 272 (2020), 118979.

[30] Z. Wang, Z. Wang, X. Zhu, C. Ai, Y. Zeng, W. Shi, X. Zhang, H. Zhang, H. Si, J. Li, C.-Z. Wang, S. Lin, Photodepositing CdS on the Active cyano groups decorated g-C3N4 in Z-scheme manner promotes visible-light-driven hydrogen evolution, Small 17 (2021), 2102699.

[31] R. Shen, X. Lu, Q. Zheng, Q. Chen, Y.H. Ng, P. Zhang, X. Li, Tracking S-scheme charge transfer pathways in Mo2C/CdS H2-evolution photocatalysts, Sol. RRL 5 (2021), 2100177.

[32] M. Wang, K. Wang, Z. Jin, Pyramidal CdS polyhedron modified with NiAl LDH to form S-scheme heterojunction for efficient photocatalytic hydrogen evolution, ChemCatChem 13 (2021) 3525–3535.

[33] Y. Yang, D. Zhang, Q. Xiang, Plasma-modified Ti3C2Tx/CdS hybrids with oxygen-containing groups for high-efficiency photocatalytic hydrogen production, Nanoscale 11 (2019) 18797–18805.

[34] D. You, D. Shi, Q. Cheng, Y. Chen, Z. Pan, Integrating Mn-ZIF-67 on hollow spherical CdS photocatalysts forming a unique interfacial structure for the efficient photocatalytic hydrogen evolution and degradation under visible light, Environ. Sci. Nano 7 (2020) 2809–2822.

[35] C. Zhang, B. Liu, W. Li, X. Liu, K. Wang, Y. Deng, Z. Guoa, Z. Lv, A well-designed honeycomb Co3O4@CdS photocatalyst derived from cobalt foam for high-efficiency visible-light H2evolution, J. Mater. Chem. A 9 (2021) 11665–11673.

[36] R. Xiao, C. Zhao, Z. Zou, Z. Chen, L. Tian, H. Xu, H. Tang, Q. Liua, Z. Lin, X. Yang, In situ fabrication of 1D CdS nanorod/2D Ti3C2 MXene nanosheet Schottky heterojunction toward enhanced photocatalytic hydrogen evolution, Appl. Catal. B Environ. 268 (2020), 118382.

[37] H. Ge, F. Xu, B. Cheng, J. Yu, W. Ho, Front cover: esterification of tertiary amides by alcohols through C−N bond cleavage over CeO2, ChemCatChem 11 (2019) 1–10.

[38] X. Li, S. Song, Y. Gao, L. Ge, W. Song, T. Ma, J. Liu, Identification of the charge transfer channel in cobalt encapsulated hollow nitrogen-doped carbon Matrix@ CdS heterostructure for photocatalytic hydrogen evolution, Small 17 (2021), 2101315.

[39] P. Zhang, D. Luan, X.W. Lou, Fabrication of CdS frame-in-cage particles for efficient photocatalytic hydrogen generation under visible-light irradiation, Adv. Mater. 32 (2020), 2004561.

[40] A.V. Stavitskaya, E.A. Kozlova, A.Y. Kurenkova, A.P. Glotov, D.S. Selishchev, E. V. Ivanov, D.V. Kozlov, V.A. Vinokurov, R.F. Fakhrullin, Y.M. Lvov, Ru/CdS quantum dots templated on clay nanotubes as visible-light-active photocatalysts: optimization of S/Cd ratio and Ru content, Chem. Eur. J. 16 (2020) 13085–13092.

[41] D. Ren, W. Zhang, Y. Ding, R. Shen, Z. Jiang, X. Lu, X. Li, In situ fabrication of robust cocatalyst-free CdS/g-C3N42D–2D step-scheme heterojunctions for highly active H2 evolution, Sol. RRL 4 (2019), 1900423.

[42] F. Liu, Z. Wang, Y. Weng, R. Shi, W. Ma, Y. Chen, Black phosphorus quantum dots modified CdS nanowires with efficient charge separation for enhanced photocatalytic H2 evolution, ChemCatChem 13 (2021) 1355–1361.

[43] S. Li, L. Wang, Y.D. Li, L. Zhang, A. Wang, N. Xiao, Y. Gao, N. Li, W. Song, L. Ge, J. Liu, Novel photocatalyst incorporating Ni-Co layered double hydroxides with P-doped CdS for enhancing photocatalytic activity towards hydrogen evolution, Appl. Catal. B Environ. 254 (2019) 145–155.

[44] L. Paramanik, K.H. Reddy, K.M. Parida, An energy band compactable B-rGO/ PbTiO3 p-n junction: a highly dynamic and durable photocatalyst for enhanced photocatalytic H2 evolution, Nanoscale 11 (2019) 22328–22342.

[45] a) P. Chen, B. Lei, X. Dong, H. Wang, J. Sheng, W. Cui, J. Li, Y. Sun, Z. Wang, F. Dong, Rare-earth single-atom La-N Charge-transfer bridge on carbon nitride for highly efficient and selective photocatalytic CO2 reduction, ACS Nano 14 (2020) 15841–15852;
b) W. Li, Q. Ma, X. Wang, X. Chu, F. Wang, X. Wang, C. Wang, Enhanced photoresponse and fast charge transfer: three-dimensional macroporous g-C3N4/ GO-TiO2nanostructure for hydrogen evolution, J. Mater. Chem. A 8 (2020) 19533–19543.

[46] Z. Zhao, H. Ren, D. Yang, Y. Han, J. Shi, K. An, Y. Chen, Y. Shi, W. Wang, J. Tan, X. Xin, Y. Zhang, Z. Jiang, Boosting nitrogen activation via bimetallic organic frameworks for photocatalytic ammonia synthesis, ACS Catal. 11 (2022) 9986–9995.